Microsc. Microanal. 11, 534–544, 2005
DOI: 10.1017/S1431927605050543

Microscopy AND Microanalysis

Atomic Structure of β-Tantalum Nanocrystallites

Karsten Tillmann,[1,2,*] Andreas Thust,[1,2] Andreas Gerber,[2] Martin P. Weides,[2] and Knut Urban[1,2]

[1]*Ernst Ruska-Centrum für Mikroskopie und Spektroskopie mit Elektronen, D-52425 Jülich, Germany*
[2]*Institut für Festkörperforschung, Forschungszentrum Jülich GmbH, D-52425 Jülich, Germany*

Abstract: The structural properties of β-phase tantalum nanocrystallites prepared by room temperature magnetron sputter deposition on amorphous carbon substrates are investigated at atomic resolution. For these purposes spherical aberration-corrected high-resolution transmission electron microscopy is applied in tandem with the numerical retrieval of the exit-plane wavefunction as obtained from a through-focus series of experimental micrographs. We demonstrate that recent improvements in the resolving power of electron microscopes enable the imaging of the atomic structure of β-tantalum with column spacings of solely 0.127 nm with directly interpretable contrast features. For the first time ever, we substantiate the existence of grain boundaries of 30° tilt type in β-Ta whose formation may be well explained by atomic agglomeration processes taking place during sputter deposition.

Key words: β-tantalum, magnetron sputter deposition, thin films, grain boundaries, high-resolution transmission electron microscopy, spherical aberration correction, exit-plane wavefunction reconstruction

Introduction

Ion beam and magnetron sputtered tantalum thin films can be produced in two different crystalline phases, the body-centered equilibrium phase (α-Ta) and the metastable tetragonal modification (β-Ta). Since the discovery of the latter by Read and Altman (1965) a large amount of work has been devoted to the identification of deposition conditions and substrate pretreatment procedures supporting the formation of either. Even though the exact mechanisms leading to the formation of α-Ta or β-Ta are not clearly identified, the empirical finding is that oxide substrates or materials that readily form surface oxides at room temperature and vacuum system impurities support the nucleation of the β-phase (Feinstein & Huttemann, 1973; Westwood, 1973; Hieber & Mayer, 1982).

Both phases differ notably in their structural and electrical properties (Westwood et al., 1975) and β-Ta is known to be characterized by a comparatively higher resistivity (Face & Prober, 1987; Sajovec et al., 1992). The presently resurrected interest in tantalum thin films is, however, primarily due to the ability of tantalum interlayers to promote the adhesion of copper to dielectrics (Kwon et al., 1999) as well good barrier properties against the diffusion of copper to silicon (Laurila et al., 2000; Hübner et al., 2003).

Because of the polycrystalline structure of tantalum thin films, grain boundary diffusion becomes admittedly relevant at elevated temperatures (Gupta, 1995) and molecular-dynamics simulations indicate a pronounced anisotropic migration behavior of vacancies mediating diffusion processes in β-Ta (Klaver & Thijsse, 2002). Understanding the fundamental growth phenomena and the local structure of β-Ta crystallites is, hence, directly related to the technological relevance for thin film applications. In addition, tantalum deposition is interesting from a more fundamental point of view because of some uncertainty with respect to the most accurate model describing the atomic structure of the β-phase. In the past, a number of X-ray powder diffraction (XRD) analyses focused on the accurate determination of unit-cell parameters together with the space group of the β-phase. Moseley and Seabrook (1973) reported on an isomorphous β-uranium structure, that is, on the space group $P4_2/mnm$ with unit-cell parameters of $a = 1.0194$ nm and $c = 0.5313$ nm. More recent XRD data by Arakcheeva et al. (2002) suggest a $P42_1m$ structure with $a = 1.0194$ nm and $c = 0.5313$ nm for β-phase single crystals whereas extended X-ray absorption fine structure (EXAFS) measurements by Jiang et al. (2003) corroborate the β-uranium structure model.

Previous transmission electron microscopy (TEM) investigations mainly delved into phase identification together with the determination of the grain size and the orientation of β-phase crystallites in dependence on the deposition conditions chosen (e.g., Hieber & Mayer, 1982; Face & Prober, 1987; Sajovec et al., 1992). Nonetheless, the atomic structure of β-phase tantalum has so far not been directly imaged and, hence, no experimental data are available on lattice defects and especially on the interface structure between adjacent crystallites.

Received June 9, 2004; accepted January 18, 2005.
*Corresponding author. E-mail: k.tillmann@fz-juelich.de

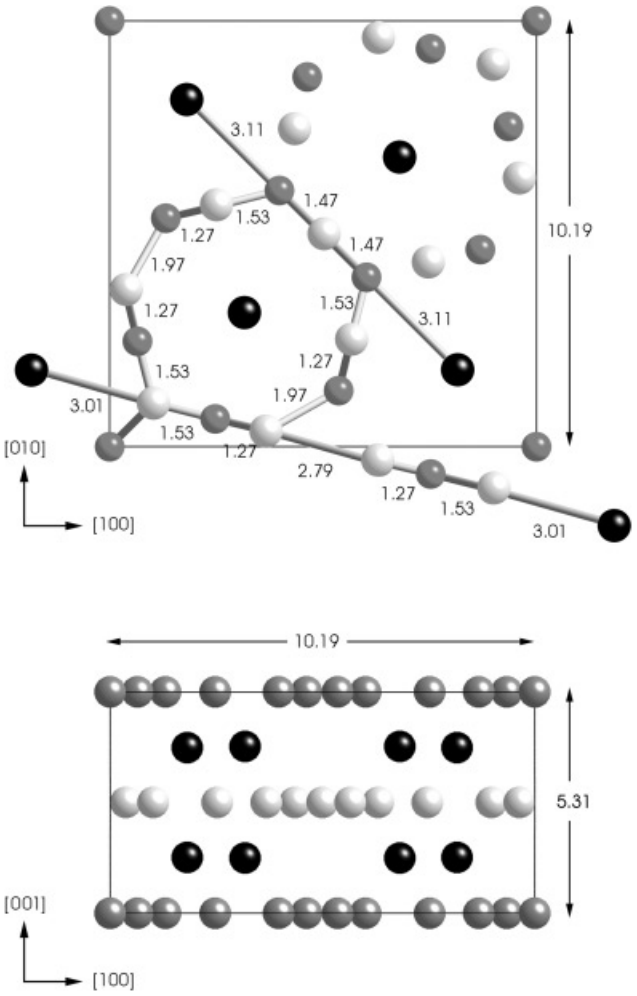

Figure 1. Tetragonal β-tantalum unit-cell ($P4_2/mnm$) according to the Moseley and Seabrook (1973) structure model as viewed along the crystallographic [001] and [010] directions, respectively. The structure can be thought of as 22 atoms forming a pair of pseudo-hexagonal planes of different rotational orientation together with 8 atoms lying halfway between these planes. In the figure, these pseudo-hexagonal planes are formed by the darker and lighter gray atoms located at positions $z = 0$ and $z = c/2$ along the [001] unit-cell axis, respectively, whereas black atoms lie in the intermediate planes at $z = c/4$ and $z = 3c/4$. When viewed along the [001] direction, the black atom positions represent doubly occupied columns with two atoms spaced one above the other per unit-cell, whereas the grayish labeled columns are singly occupied. In this projection, the atoms belonging to the pseudo-hexagonal planes appear as septagons when connected by closed trajectories of straight lines. Each of these septagons encloses a doubly occupied tantalum column. The spacings indicated between adjacent atom columns represent projected distances given in Ångström (0.1 nm) unit lengths.

This missing information, also conducive to the understanding of thin film growth processes, is primarily due to β-Ta column spacings of 0.127 nm drawn in the [001] unit-cell projection displayed in Figure 1 and assuming the Moseley and Seabrook (1973) structure model.[†] Such small distances so far could not be resolved with commercially available medium-voltage electron microscopes limited by a point-to-point resolution of about 0.17 nm at directly interpretable image contrast features.

However, sophisticated instrumental concepts, that is, double hexapole corrector elements (Haider et al., 1998), combined with the tuning of the microscope objective lens toward a slightly negative spherical aberration, also yielding pronounced bright-atom image contrast features in line with a low image delocalization (Jia et al., 2004), allow extension of the point resolution to the information limit $1/g_{max} = 0.125$ nm of field emission gun instruments operated at an accelerating voltage of only 200 kV. Moreover, numerical retrieval techniques enable accurate extraction of the complex-valued exit-plane wavefunction from a through-focus series of high-resolution images (Coene et al., 1996; Thust et al., 1996*a*). By this means, all spatial information up to the information limit of the instrument can be retrieved, also allowing for a subsequent elimination of residual lens aberrations (Thust et al., 1996*b*, 2002; Tillmann et al., 2004).

The purpose of the present study is to obtain atomic-level information on the structure of β-Ta crystallites. More specifically, we investigate for the first time β-phase tantalum nanocrystallites formed upon room temperature magnetron sputter deposition on amorphous carbon substrates at atomic resolution. Experimental analyses are performed using both a spherical aberration-corrected 200-kV instrument together with the numerical retrieval of the exit-plane wavefunction from a through-focus series of micrographs. We demonstrate that the atomic-scale characterization of β-Ta nanoclusters allows for the identification and comprehensive structural analysis of 30° tilt boundaries whose formation may be well explained by agglomeration processes taking place during sputter deposition.

Experimental and Instrumental Setup

Tantalum coatings with nominal thicknesses d_{nom} between 5 nm and 30 nm were deposited on thin amorphous carbon films (≈30 nm) that were suspended on standard 400-mesh copper grids. These grids were centered on a 4-in. aluminum plate that was transferred via load-lock and manipula-

[†]From an electron microscopy point of view, the structure models proposed by Moseley and Seabrook (1973) and by Arakcheeva et al. (2002) are nearly identical when the material is viewed along the [001] zone axis. Both structures differ only in the respect that the latter model considers a minor lateral shift of those two atoms forming the doubly occupied columns, labeled black in Figure 1, against each other. Because numerical image simulations demonstrate that this small displacement does not have any impact on the high-resolution image contrast, within the framework of this study we presume the Moseley and Seabrook (1973) model to be correct.

tors to the water-cooled substrate holder of a Leybold Univex 450B magnetron sputtering system. The water cooling together with a relatively low sputter rate provided room temperature deposition conditions.

The sputter deposition was performed at a background pressure of $5 \cdot 10^{-7}$ mbar with a target-to-substrate distance of 7 cm. When applying DC power of 75 W together with a sputter pressure of $5 \cdot 10^{-3}$ mbar of argon gas (purity 5.6), as were chosen in this study, these standard conditions produce a deposition rate of 0.5 ± 0.05 nm s^{-1} for tantalum thin films. This sputter rate was verified by thickness measurements on reference samples using a Dektak profiler. Tantalum targets (purity 99.95%) of 4-in. diameter were used and a computer-controlled shutter system was applied to regulate the sputter time and, hence, the nominal layer thickness. The sputter process involved a presputtering step of the tantalum target at 150 W for 30 s with the shutter closed to eliminate impurities. After sputtering, the argon gas flow was continued for 30 s to enhance the cooling by using argon as an exchange gas between the substrate holder on the copper grids.

To remove the amorphous carbon support film, electron transparent samples for use during conventional TEM and electron diffraction experiments were subjected to a 30-min plasma cleaning procedure from the carbon film side applying a Binder TPS 216 system. This was followed by a cleaning step from the tantalum coating side of the samples for 4 min. As was verified in the framework of a preliminary inspection of uncoated standard 400-mesh copper grids, already the first 30 min cleaning step resulted in a complete removal of the carbon support film.

Samples for use during high-resolution experiments were prepared by combined ion etching and plasma cleaning also applying a Gatan Duo Ion Mill Model 600 system. For these purposes samples with $d_{\mathrm{nom}} = 12$ nm were at first subjected to an Ar^+ ion-etching step from the tantalum coating side of the samples applying an ion energy of 2 keV at a beam current of 0.5 A for $\tau = 30$ s. To remove the main part of the amorphous carbon film, the samples were finally subjected to the very same 30-min plus 4-min plasma cleaning step as specified previously. By systematically increasing the ion-etching period τ at otherwise fixed conditions, it was found that both the metallic glance of the tantalum coating as well as the Debye-Scherrer fringes visible in the diffraction patterns disappeared at about $\tau_d \approx 50$ s, thus indicating the complete removal of the tantalum coating. In view of an additional etching contribution from the plasma cleaning step we may, hence, presume that the effective thickness of these specimens is $t = (1 - \tau/\tau_d) d_{\mathrm{nom}} = 4.8$ nm at most.

The investigation of the basic coating structure and the phase identification of the tantalum coating were performed by transmission electron microscopy and electron diffraction using a magnification calibrated Philips CM-200 FEG ST microscope operated at an accelerating voltage of 200 kV, that is, at an electron wavelength of $\lambda = 2.508$ pm. High-resolution micrographs were taken with the instrument's objective lens adjusted toward a negative constant of spherical aberration, as introduced by Lentzen et al. (2002) and Jia et al. (2004), given by

$$C_{\mathrm{S}} = -64/27\ (\lambda^{-3} g_{\mathrm{max}}^{-4}) = -40\ \mu\mathrm{m}, \tag{1}$$

with $1/g_{\mathrm{max}} = 0.125$ nm denoting the information limit. With this setting an overfocus value

$$Z_{\mathrm{opt}} = 16/9\ (\lambda^{-1} g_{\mathrm{max}}^{-2}) = 11.6\ \mathrm{nm} \tag{2}$$

yields directly interpretable high-resolution micrographs characterized by pronounced bright-atom contrast features and accompanied by a residual image delocalization of

$$R = 16/27\ g_{\mathrm{max}}^{-1} = 0.08\ \mathrm{nm}. \tag{3}$$

Instrumental fine-tuning operations have been carried out as described in a previous study (Tillmann et al., 2004). Through-focus series of micrographs were recorded using a $1\mathrm{k} \times 1\mathrm{k}$ charge-coupled device (CCD) camera system, choosing magnification settings that ensured a sampling rate of about 13 pm per picture element, that is, an image discretization well below the Nyquist frequency with respect to half of the information limit $1/(2g_{\mathrm{max}}) = 65$ pm of the electron microscope.

Basic Structure of the Tantalum Coatings

Prior to the atomic-scale imaging of the tantalum coatings, all samples were subjected to a basic structural analysis to gain information on the average size of the crystallites and on the tantalum phase formed upon sputter deposition.

The bright-field micrograph displayed in Figure 2a, which was taken from a plan-view sample with $d_{\mathrm{nom}} = 12$ nm subjected to the plasma cleaning procedure specified before, already reveals the polycrystalline structure of the tantalum coating as expressed by the granular image contrast. Similar contrast features have also been observed by Hieber and Mayer (1982), focusing on the structure of tantalum films on Corning glass and by Face and Prober (1987) analyzing β-Ta coatings deposited on amorphous carbon. Bright-field micrographs taken from the sample displayed in Figure 2a at higher magnification reveal randomly oriented lattice fringes all over the specimen area under investigation. These fringes, although rather faint in contrast to some extent, thus, reveal a continuous tantalum coating.

The origin of the bright-field image contrast behavior of the micrograph displayed in Figure 2a is of a twofold nature. On the one hand, the different orientations of the crystallites with respect to the electron beam direction in-

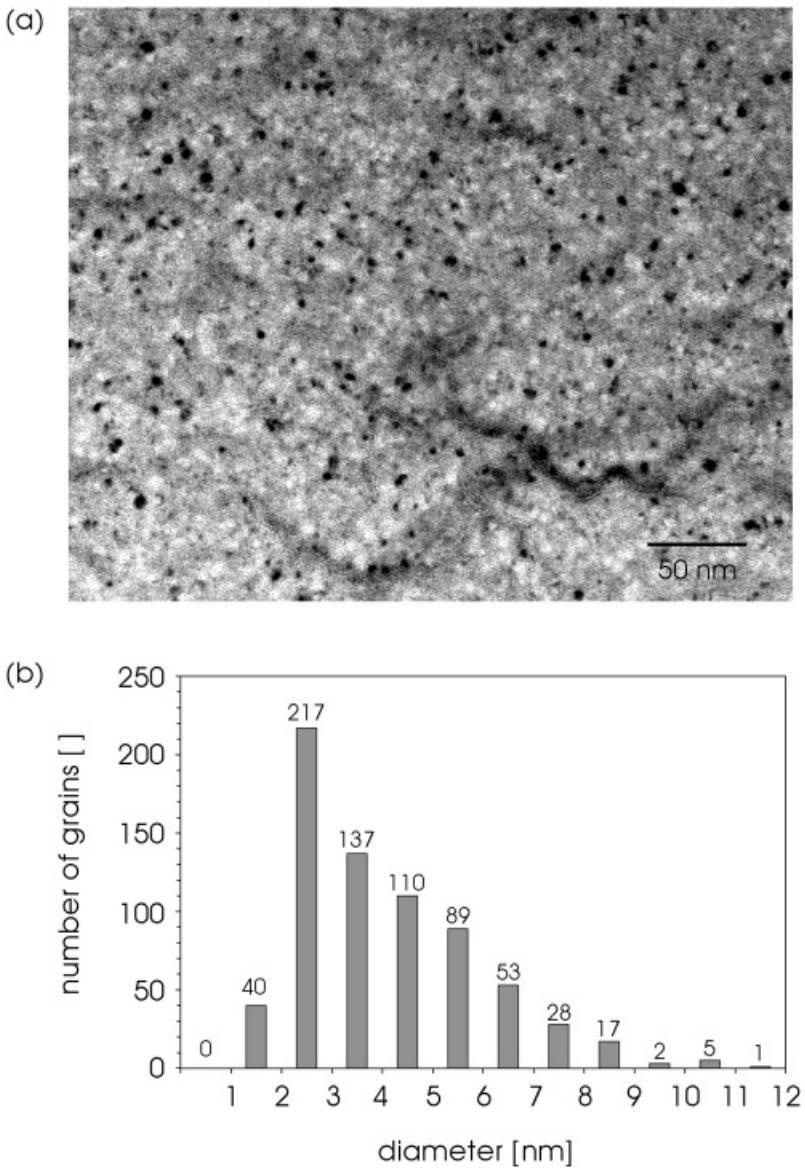

Figure 2. a: Bright-field electron micrograph taken from a plan-view sample with d_{nom} = 12 nm. Depending on their crystallographic orientation with respect to the incident electron beam as well as their thickness in relation to the extinction distance, individual strongly scattering nanocrystallites appear either black or white in contrast whereas weakly scattering crystallites give rise to the gray background contrast. **b:** Equivalent circular diameter distribution evaluated from the bright-field micrograph by measuring those crystallites appearing black in contrast.

duce pronounced local variations in the excitation of the transmitted electron beam and, hence, give rise to intensity variations within the bright-field micrograph. On the other hand, in view of relatively small extinction distances of the transmitted beam, for example, $\xi_0 = 8$ nm and 13 nm along the [001] and [010] directions, minor variations in the grain size will result in different image intensities of crystallites of the same crystallographic orientation (Hirsch et al., 1965).

However, leaving aside the exact origin of these contrast motifs and using standard particle analysis routines embedded in the DigitalMicrograph software package (Gatan Inc, 1999) involving the thresholding of the image intensity followed by the measurement of specific particle properties, an equivalent circular crystallite diameter distribution according to Figure 2b is obtained from the micrograph shown in Figure 2a. The distribution shows that the crystallite sizes are well below 10 nm, with an average equivalent diameter of $d = 3.53 \pm 1.09$ nm at a coating thickness of $d_{nom} = 12$ nm.

Similar results are obtained for other nominal layer thicknesses with a tendency toward larger grain sizes at increased coating thicknesses. Corresponding measurements yield $d = 2.82 \pm 1.22$ nm ($d_{nom} = 5$ nm) and $d = 6.41 \pm 1.52$ nm ($d_{nom} = 30$ nm). This development is in line with previous TEM analyses by Sajovec et al. (1992) demonstrating grain sizes of $d = 7.9 \pm 2.5$ nm at $d_{nom} = 50$ nm for β-Ta coatings deposited under similar conditions. Assuming roughly spherical crystallites, these d values are tantamount to approximately two ($d_{nom} = 5$ nm) to six ($d_{nom} = 50$ nm) grains lying upon each other along the normal of the samples.

From the analysis of selected area diffraction patterns, it is found that all tantalum films nucleate in the tetragonal

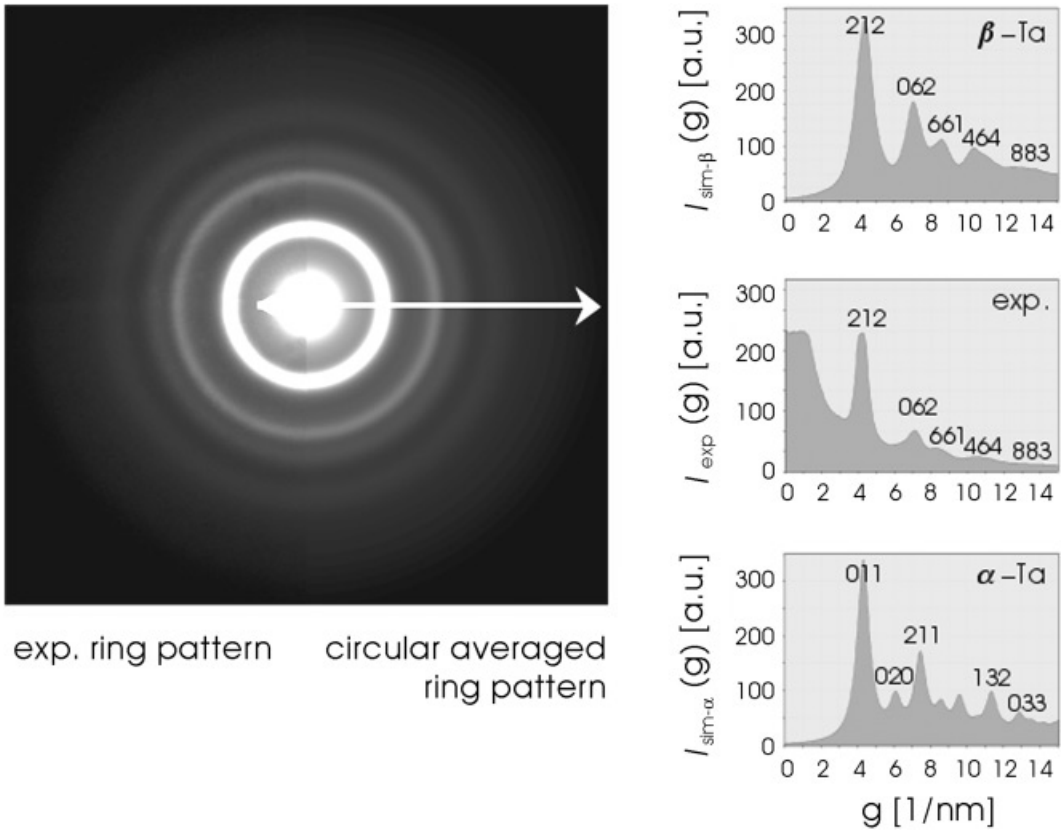

Figure 3. Split-up representation of an experimental diffraction pattern obtained from a plan-view sample (d_{nom} = 12 nm) together with a circularly averaged pattern. Extremal positions of the experimental intensity line profile $I_{exp}(g)$, which was taken along the direction indicated by the arrow in the circularly averaged pattern, coincide solely with simulated $I_{sim}(g)$ extremal positions assuming a β-Ta but not an α-Ta structure model.

β-phase, as exemplified by the Debye-Scherrer pattern displayed in Figure 3 and taken from the $d_{nom} = 12$ nm sample. The pattern demonstrates pronounced intensity extrema best visible in the experimental line scan $I_{exp}(g)$ extracted from the circularly averaged Debye-Scherrer pattern.

When compared with simulated intensity line profiles, as calculated by application of the EMS code (Stadelmann, 1987), and assuming a grain size of 3 nm, these extrema positions coincide solely with the β-phase structure and not with α-Ta crystallites. Deviations in the profile shapes close to $g = 0$ are due to the neglect of specimen thickness and dynamical diffraction effects in the simulations, as well as to the overexposure caused by the undiffracted beam in the experimental pattern. Similar results are obtained for the other coating thicknesses, demonstrating the exclusive formation of β-Ta crystallites.

High-resolution Imaging at Negative C_S Conditions

Figure 4 shows an experimental $Z_{opt} \approx 12$ nm image taken on the $d_{nom} = 12$ nm sample subjected to the specimen preparation procedure described before and recorded under negative spherical aberration imaging conditions. The image has been selected from a through-focus series of micrographs and shows an extended β-phase crystallite viewed along the [001] direction.

The image contrast is somewhat bleary and characterized by a less advantageous signal-to-noise ratio. This may either be due to (1) nonnegligible image contributions from the amorphous carbon substrate or from underlying misoriented tantalum atoms or grains, which may not have been completely removed by the applied specimen preparation procedures, (2) radiation damage, or (3) because of high-frequency vibrations of the copper-grid-supported sample. The latter were observed through the binoculars upon operation of the microscope. However, apart from the aforementioned bleariness, the image contrast is dominated by a number of nearly detached contrast dots surrounded by irregular septagons that are themselves composed of 12 contrast dots of comparatively lower intensity.

For cross-verification between contrast dot and atomic column positions, numerical image simulations using the macTempas package (O'Keefe & Kilaas, 1988) have been carried out. Electron-optical parameters of a spherical aberration-corrected Philips CM200 FEG ST instrument

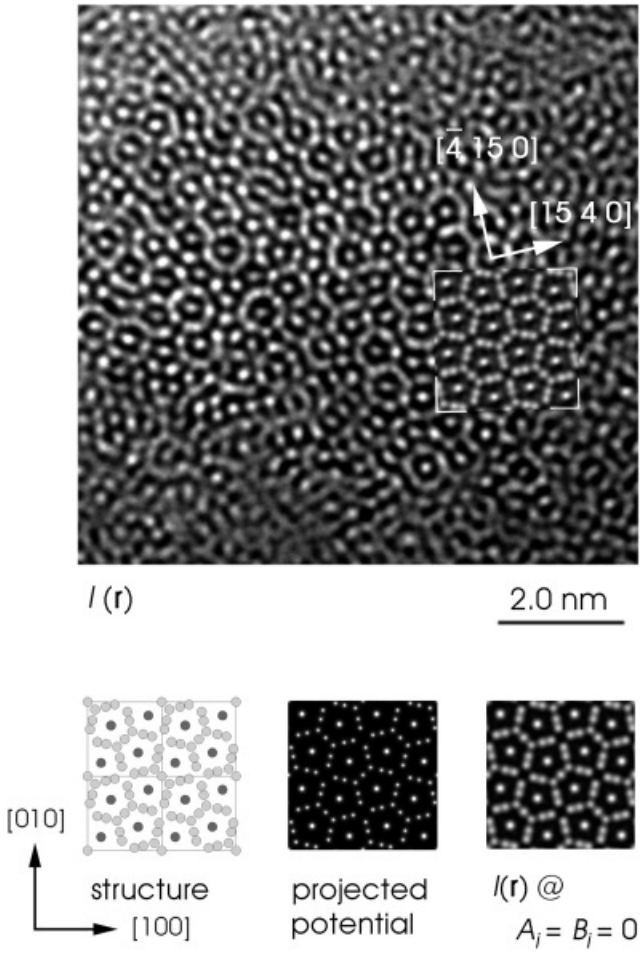

Figure 4. High-resolution electron micrograph of a β-phase tantalum nanocrystallite viewed along the [001] zone axis and recorded with $C_S = -40$ μm under optimum defocus conditions, that is, at $Z \approx 12$ nm. The 2×2 unit-cell insertion to the micrograph shows a calculated image assuming $t = 1.5$ nm, $Z = 11.6$ nm, $A_1 = 4.2$ nm (110°), $B_2 = 70$ nm (340°), and $A_2 = 120$ nm (0°) as simulation parameters. The three images below the micrograph display the corresponding structure model together with the projected potential map and a calculated image assuming $A_1 = B_2 = A_2 = 0$ at otherwise fixed calculation parameters.

operated under negative C_S conditions have been chosen, that is, $C_S = -40$ μm for the coefficient of spherical aberration, 0.2 mrad for the semi-angle of beam convergence, and 6.4 nm for the 1/*e*-half-width of the Gaussian spread of defocus. An absorption constant of 0.04 and a Debye–Waller factor of 0.006 nm^2 were employed for the tantalum atoms. Mechanical instabilities of the instrument were taken into account by setting the Gaussian half-width parameters for mechanical vibrations perpendicular and parallel to the side-entry holder axes to 0.03 nm and 0.04 nm, respectively. Multislice calculations with a slice thickness of 0.05 nm were used to calculate the exit-plane wavefunction and subsequent high-resolution images.

The corresponding calculated 2×2 unit-cell clipping is superimposed on the experimental micrograph displayed in Figure 4. Calculations assume a sample thickness $t = 1.5$ nm together with residual parasitic aberrations of $A_1 = 4.2$ nm (110°), $A_2 = 120$ nm (10°), and $B_2 = 70$ nm (340°) for the two- and threefold astigmatism as well as for the axial coma, respectively. The values in parentheses indicate azimuth angles inclined with the horizontal image axis also representing the crystallographic [100] direction in respect to the simulations.[‡] As can be seen from a direct comparison with the experimental micrograph, relevant contrast features are in good agreement with each other on a relative scale.

When compared with the β-Ta structure model or the projected potential map, both displayed in 2×2 unit-cell representations on the bottom left and middle in the figure, it becomes evident that the central bright dot positions in the micrograph are directly linked to the doubly occupied tantalum columns whereas the enclosing septagons cover the singly occupied columns appearing at comparatively decreased image intensity values. The direct comparison, thus, provides clear evidence for the experimental realization of bright-atom imaging conditions.

However, minor contrast pattern asymmetries such as the elliptical distortion of the central contrast dots and the increased blurring of the septagon-related contrast feature along the [15 4 0] direction compared to the orthogonal [$\bar{4}$ 15 0] direction are visible in the experimental, likewise calculated, images. These distortions will be primarily due to the residual lens aberrations as they are absent in simulated images when assuming $A_1 = A_2 = B_2 = 0$ at otherwise fixed calculation parameters (cf. the image displayed on the bottom right of Figure 4). This finding demonstrates that proper control of the residual aberrations and an improved long-term stability of the instrumental setup will play a key role when operating future-generation microscopes at the verge of the information limit.

Whether considering the residual aberrations or not, the experimental micrograph's resolution displayed in Figure 4 is slightly below the predictions of the corresponding image simulations. As far as numerical calculations are concerned, this observation will be due to the neglect of the aforementioned residual image contributions originating from ultrathin carbon or tantalum coatings covering the crystallite under investigation as well as because of the neglect of radiation damage in the simulations. Additionally, a minor misorientation of the crystallite, as may be anticipated from the exiguous asymmetry of the experimental diffraction pattern displayed in Figure 8a below, will effectively reduce the resolution of experimental micrographs as atomic columns converge in projection. Because crystal tilt is a synonym for an effectively lower projected

[‡]The specified aberrations follow directly from the retrieval of the exit-plane wavefunction as will be discussed in the next section.

potential, additional image simulations have been carried out. These calculations, however, demonstrate that specimen thickness values in the range 2 nm $\leq t \leq$ 12 nm $= d_{\mathrm{nom}}$ will not reproduce the experimental Z_{opt} micrograph, as the rather small extinction distances of major reflections give rise to contrast patterns quintessentially different from that of the experimental micrograph.

Retrieval of the Exit-Plane Wavefunction

Figure 5 displays the phase $\Phi(\mathbf{r})$ and amplitude $A(\mathbf{r})$ of the exit-plane wavefunction as retrieved from the through-focus series of 15 micrographs taken in the focal range 40.0 nm $\geq Z \geq -5.5$ nm at an increment of $\Delta Z = 3.25 \pm 0.03$ nm. The reconstruction process involved the measurement of the twofold astigmatism A_1 from the signal of amorphous specimen areas followed by the simultaneous refining of the symmetry properties of different object areas under investigation as methodically described by Thust et al. (2002) and by Tillmann et al. (2004) and allowing for the measurement of the odd aberrations, for example, the axial coma B_2 and the threefold astigmatism A_2. Corresponding operations yield $A_1 = 4.2$ nm (110°), $B_2 = 70$ nm (340°), and $A_2 = 120$ nm (10°), with the values in parentheses indicating respective azimuth angles inclined with the horizontal image axis. The phase and amplitude images displayed in the figure are already numerically corrected by these values.

Whereas $\Phi(\mathbf{r})$ shows clearly separated and distinctly peaked intensity values at the tantalum columns, the retrieved $A(\mathbf{r})$ image demonstrates decreased amplitude values at these positions. Both experimental images, $\Phi(\mathbf{r})$ and $A(\mathbf{r})$, coincide well with the simulated image insertions added to the figure and representing projected 2×2 unit-cell clippings. The images clearly demonstrate locally increased ($\Phi(\mathbf{r})$) and decreased ($A(\mathbf{r})$), respectively, intensities at the doubly occupied column positions compared to the singly occupied septagon positions. Simulation parameters are identical to those specified in the previous section. The experimental phase and amplitude are, however, characterized by an inferior signal-to-noise ratio when compared to the calculated images. As before, this behavior will be due to a certain noise contribution from leftovers of the amorphous carbon substrate or because of substantial specimen vibrations during recording of individual images of the through-focus series. Clearly, not even sophisticated numerical techniques can retrieve the intrinsic specimen structure when the structural details can only be recorded under slightly blurred conditions.

However, with regard to the comparison of relevant contrast features, intensity line profiles extracted from experimental and calculated images along certain directions x represent a convenient tool. Corresponding profiles $A(x)$

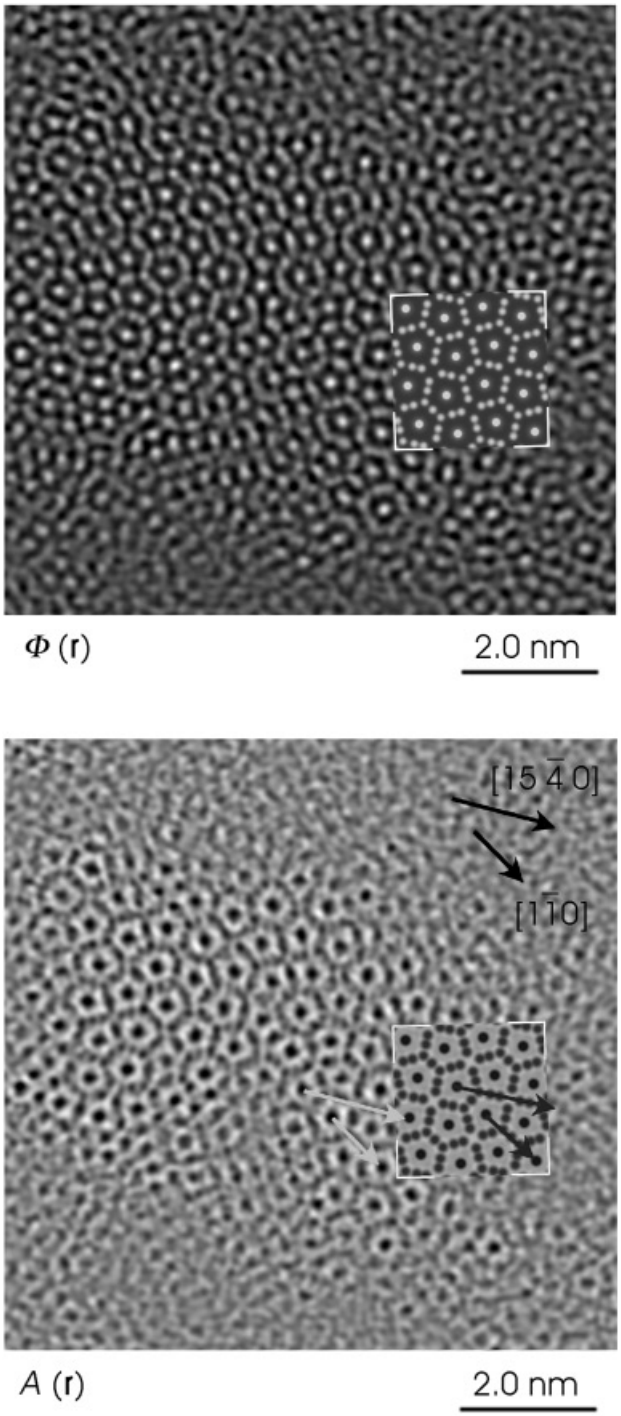

Figure 5. Experimental phase $\Phi(\mathbf{r})$ and amplitude $A(\mathbf{r})$ of the exit-plane wavefunction evaluated from a through-focus series of 15 images. The insertions show simulated images $\Phi(\mathbf{r})$ and $A(\mathbf{r})$ assuming a sample thickness of $t = 1.5$ nm at otherwise fixed simulation parameters. The two pairs of lighter and darker gray arrows along the [15 $\bar{4}$ 0] and [1 $\bar{1}$ 0] directions indicate positions at which intensity line profiles displayed in Figure 6 have been extracted from the experimental, likewise simulated, images.

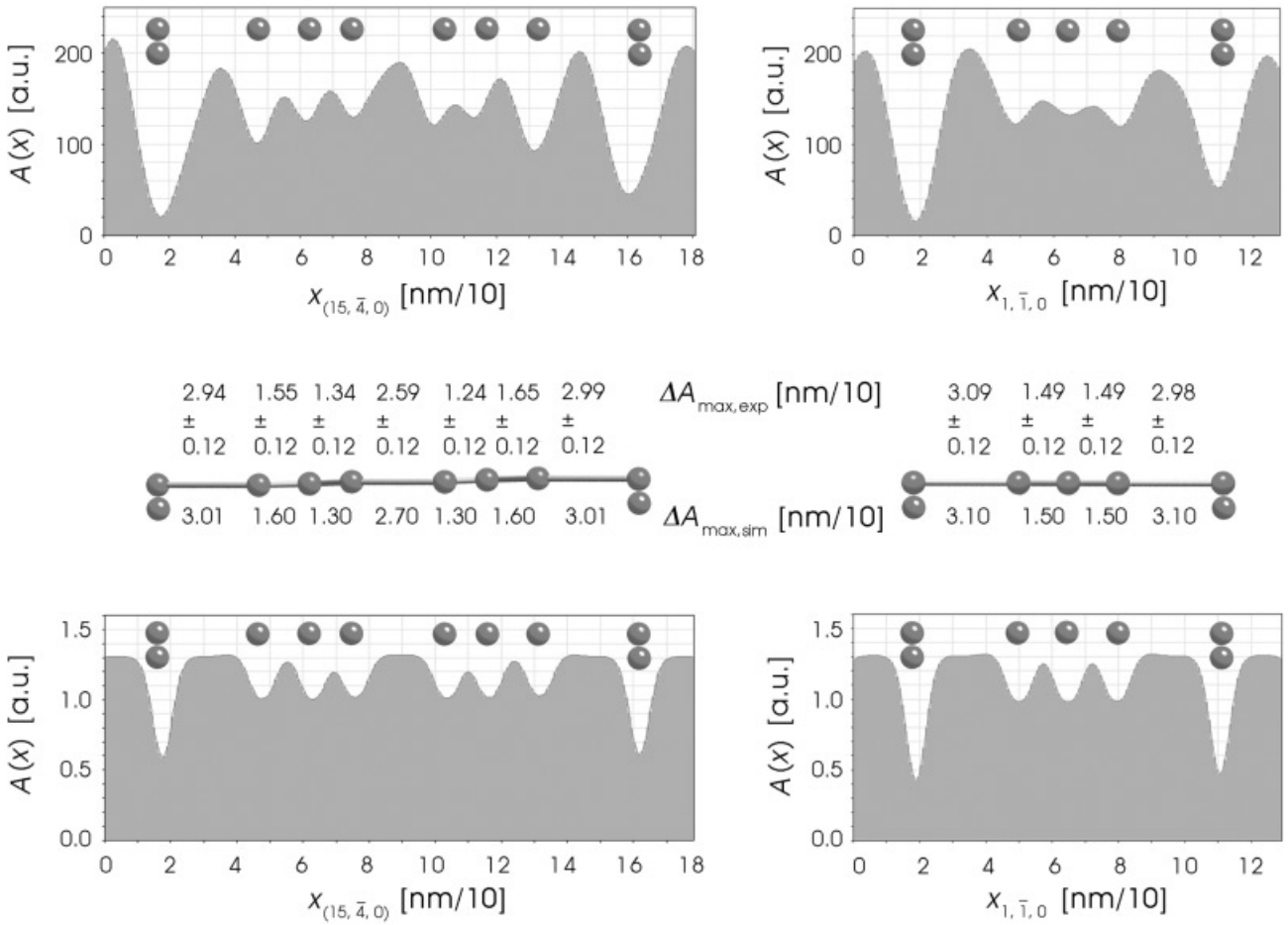

Figure 6. Amplitude line profiles $A_{exp}(x)$ and $A_{sim}(x)$ extracted from the experimental and simulated areas of the $A(\mathbf{r})$ image displayed in Figure 5, respectively. The profiles cover the crystallographic $[15\ \bar{4}\ 0]$ and $[1\ \bar{1}\ 0]$ directions. In each profile, the number of atoms drawn in at the amplitude extrema positions indicates the occupancy of the corresponding column. Numerical data on spacings Δx_{exp} and Δx_{sim} between adjacent amplitude minima positions have been extracted from displayed $A_{exp}(x)$ and $A_{sim}(x)$ profiles.

measured from the amplitude of the exit-plane wavefunction along the $x = [15\ \bar{4}\ 0]$ and $x = [1\ \bar{1}\ 0]$ directions are displayed in Figure 6. The line profile positions with respect to the $A(\mathbf{r})$ image are drawn as two pairs of lighter (experimental) and darker gray (calculated) arrows in Figure 5, each indicating the aforementioned crystallographic directions in β-phase tantalum viewed along the [001] zone axis. Owing to the symmetry properties of the crystal, $A(x)$ profiles taken along these two directions cover the entirety of spacings between the singly occupied columns of the septagon substructure. The profile positions are chosen in such a way that they also traverse the doubly occupied column close to the starting and terminating points of the profiles. Upon evaluation, the profiles have been averaged perpendicular to the line direction over a width of three pixels each, that is, over an image area of 0.039 nm in width, for the improvement of the signal-to-noise ratio.

In general, paired profiles $A_{exp}(x)$ and $A_{sim}(x)$ coincide well on a relative level, although absolute amplitude values and profiles shapes are not in precise accordance. This is especially true in view of a lateral narrowing of high amplitude plateau areas, which appear more peaked in the experimental profiles (cf. the shapes between the most outer doubly occupied tantalum columns positions along both the $x = [15\ \bar{4}\ 0]$ and $x = [1\ \bar{1}\ 0]$ directions). In other words, the comparison of the steepness of profiles $A_{exp}(x)$ and $A_{sim}(x)$ in the vicinity of these doubly occupied column positions reveals that the simulated profiles are characterized by a slightly higher resolution compared to the experimental data. An all-embracing discussion of this observation, which may be due either to a minor crystal tilt smearing out the projected potential or because of the aforementioned vibrations of the sample or the residual image delocalization of $R \approx 0.08$ nm still present in spherical aberration-corrected microscopy (Lentzen et al., 2002) together with the well-known factor-of-three difference in image contrast between experimental and simulated images (Hÿtch & Stobbs, 1994; Boothroyd, 1998), is, however, beyond the scope of this study.

All line profiles demonstrate clearly peaked amplitude minima at the atomic column positions. Column spacings Δx_{exp} and Δx_{sim} as obtained from the measurement of extrema positions in the $A_{exp}(x)$ and $A_{sim}(x)$ profiles, respectively, are also displayed in the center of Figure 6. Specified error values represent uncertainty intervals due to the discretization of the corresponding images. Both Δx_{exp} and Δx_{sim} values thoroughly coincide to a large extent, thus confirming a point-to-point resolution of at least 0.13 nm at directly interpretable amplitude images.

When compared to the singly occupied tantalum columns, distinctly decreased amplitude values are observed in all profiles at the doubly occupied columns. This observation is directly linked to the increased projected scattering potential and may be interpreted as a kind of occupancy-sensitive imaging mode. The generalization of this observation toward arbitrary diffraction conditions or even for quantification purposes is, however, far from straightforward because conspicuous image artefacts, for example, wrap-around effects, are observed at increased specimen thicknesses.

Materials-Science-Related Considerations

Finally, the data gained so far is applied to a discussion of materials-science-related aspects of the defect structure and on the mechanisms of crystallite growth upon magnetron sputtering deposition of β-phase tantalum coatings on amorphous carbon substrates. Due to the atomic-resolution capabilities of the analysis techniques, we may directly associate doubly occupied tantalum columns in the amplitude image with the stronger dark contrast dots and singly occupied columns with the weaker dot positions.

In Figure 7, the latter are superimposed on the retrieved amplitude $A(\mathbf{r})$ image with each black dot indicating a singly occupied tantalum column. When virtually joining together these dots to septagons, each of these substructures encloses a doubly occupied tantalum column. In the figure, individual [001] unit-cell edgings, as indicated by the lighter gray squares, are additionally superimposed on the $A(\mathbf{r})$ image. By this means, it becomes evident that the crystalline region of the sample is composed of four areas of different in-plane orientation. These four grains, which are highlighted by different colors, are rotated against each other by variable multiples of approximately 30°, as sketched by the auxiliary unit-cell frames added to the figure. The lighter gray unit-cell edgings also reveal some elastic strain in the grains as the black dots nearest the unit-cell corners lie at slightly differing distances from these corners.

The three grains highlighted in red, blue, and orange are each rotated by 30° with respect to the adjacent grains at a common (001) plane orientation, thus proving the existence of asymmetric 30° tilt grain boundaries of type

$$(0\,0\,1)_\alpha \,||\, (0\,0\,1)_\beta \quad \text{and} \quad [0\,1\,0]_\alpha \,||\, [\bar{1}\,\sqrt{3}\,0]_\beta \qquad (4)$$

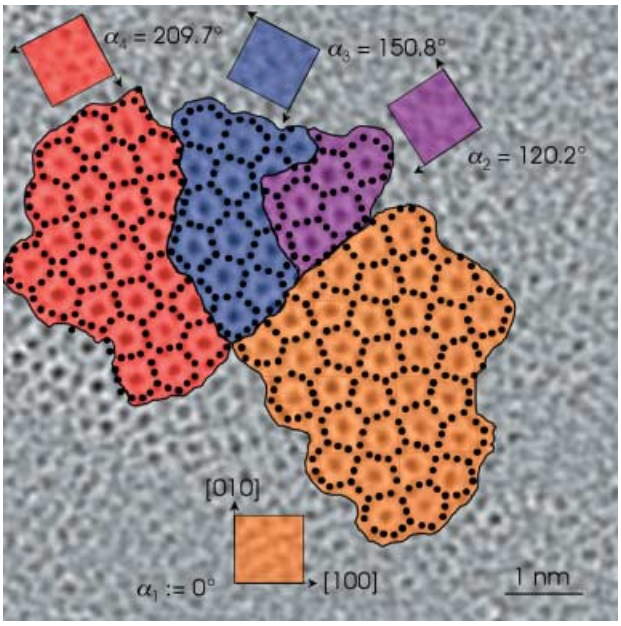

Figure 7. Amplitude image $A(\mathbf{r})$ according to Figure 5 with the positions of the singly occupied tantalum columns superimposed (•) and the borders of the unit-cells indicated by faint gray squares. The nanocrystallite as a whole is found to be composed of four grains highlighted by different colors and rotated against each other by multiples of 30°.

with α and β denoting neighboring grains. In spite of the uniform 30° tilt properties, a common likewise uniform habitat plane cannot be assigned to all three boundaries. However, most boundary segments run along directions that satisfy the principle that the atomic columns in the adjoining grains have closely similar patterns and spacings at the common boundary. Main boundary segment directions cover the crystallographic ⟨100⟩ and ⟨110⟩ directions as can be seen from the interface structure between the orange and the violet grains, which shows local mirror symmetry with respect to the habit plane. Larger amorphous areas between adjacent grains are not observed. The same finding is true for the boundary between the orange and blue grains as well as for most areas in the vicinity of the boundary between the red and blue grains.

The multiple of 30° orientation relationship between the four grains is corroborated by an observation that results as a side issue of the retrieval of the exit-plane wavefunction. Because the reconstructed exit-plane wavefunction is complex valued, we may easily evaluate "local" diffraction patterns[§] from the specimen area under investi-

[§] "Local" refers to the image area of only 9 nm × 9 nm as opposed to conventional TEM diffraction patterns that gather structural information from a specimen area selected by the selected area aperture. Moreover, it is emphasized that a "diffraction pattern" perpetuates potential asymmetries between pairwise opposite reflections whereas a "power spectrum" as obtained by the Fourier transform of real-valued high-resolution images does not contain this information.

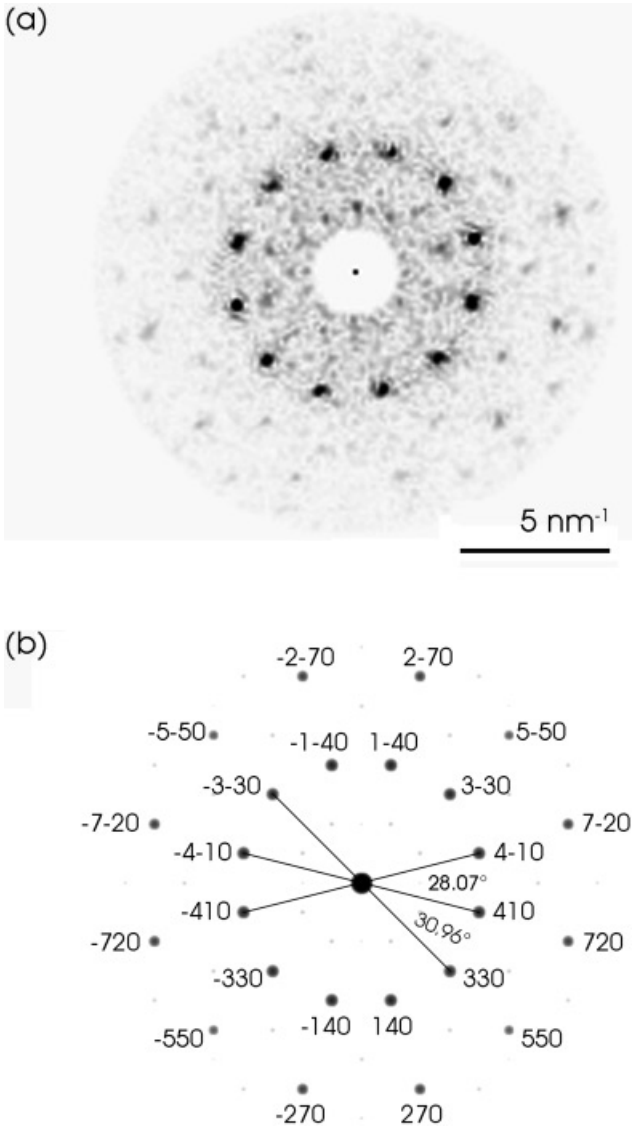

Figure 8. Local diffraction pattern (**a**) obtained from the experimental exit-plane wavefunction displayed in Figure 5 together with (**b**) a calculated diffraction pattern of monocrystalline β-tantalum assuming a sample thickness of 1.5 nm and an [001] zone axis orientation of the sample. The experimental pattern shows faintly increased spot intensities to the lower right, which may be due to fragmentary unit-cells defining the margin of the laterally limited crystallite, thus representing a boundary value problem resulting in the overemphasis of certain reflections, but also because of a minor crystal tilt of the total nanocrystallite.

gation (Thust et al., 2002; Tillmann et al., 2004). Figure 8a shows an extracted pattern evaluated from the phase and amplitude images displayed in Figure 6. The pattern shows pronounced 12-fold symmetry as would also be expected for monocrystalline β-tantalum, whose simulated diffraction pattern is displayed in Figure 8b.[¶] Calculations assume a sample of 1.5 nm in thickness viewed along the [001] zone axis. Taking into account the polycrystalline nature of the total nanocrystallite, the extensive coincidence of both patterns can thus only be explained by an arrangement of grains rotated by multiples of 30° against each other.

This nearly precise 30° rotational relationship between adjacent grains allows some insights with respect to the nucleation process of the nanocrystallite. Condensation from the vapor phase occurs through heterogeneous nucleation and subsequent growth on the substrate surface. At later stages of growth, different nuclei eventually impinge on each other and, thus, form grain boundaries. When four initially isolated nuclei undergo such a coalescence process it is, however, extremely unlikely that these grains will have already started growing with mutual multiples of 30° rotational orientation on an amorphous substrate. From a probability point of view, this hypothetical process is on a level with the spontaneous rotational realignment of monolithic grains of some nanometers in size immediately before grains coalesce. Due to the dedicated activation energy associated with such an integrative *ad hoc* rotation (Venables et al., 1984) we may rule out both of these potential boundary formation mechanism.

Instead, a more reasonable explanation would be that the 30° tilt boundaries are directly grown in at the free surfaces of laterally expanding grains, which involves the adsorption of tantalum atoms at misaligned unit-cell positions. A similar behavior is well known from complex-unit-cell materials characterized by a rather low next-nearest-neighbor interaction, likewise for low surface mobility deposition conditions (Stokes & Evans, 1997). In this respect, it is of no importance whether the trapped atoms impinge directly from the vapor or if they are detached from any cluster and migrate via surface diffusion to an adjacent grain. Due to a certain amount of energy transfer from impinging atoms these processes may even take place upon room temperature sputtering of metal systems (Abelmann & Lodder, 1997). The direct grain-boundary formation during adsorption is also corroborated by the experimentally observed existence of mirror-symmetric habit planes and the absence of twist components between all four grains and, especially, by the absence of thin amorphous interspacings between adjacent grains.

[¶]In the strict sense, the diffraction pattern of the tetragonal β-phase shows fourfold symmetry when viewed along the [001] zone axis because the radial positions of the (330) and the (140) spots differ by $1 - \sqrt{17/18}$, that is, by less than 3%. The inclined angles between adjacent (330) and (410) as well as (410) and (4$\bar{1}$0) reflections amount to 30.96° and 28.07°, respectively. We neglect this minor difference, which cannot be measured from the rather noisy experimental electron diffraction pattern displayed in Figure 8a.

Conclusions

In summary, a combination of spherical aberration-corrected high-resolution transmission electron microscopy and the numerical retrieval of the exit-plane wavefunction has been applied to the atomic-scale investigation of β-tantalum nanocrystallites. Coatings have been deposited by magnetron sputter deposition on amorphous carbon substrates under room temperature conditions.

It has been demonstrated that recent improvements in the resolution power of transmission electron microscopes enable the imaging of β-tantalum with column spacings of only 0.127 nm with directly interpretable contrast features. Moreover, the widely minimized image delocalization also allowed for the atomic-scale characterization of lattice defects associated with tantalum nanocrystallites. These crystallites were found to be composed of grains rotated against each other inside a common (001) plane and separated by asymmetric 30° tilt boundaries with mainly ⟨100⟩ and ⟨110⟩ segment directions. The formation of these boundaries may be well explained by considering atomic mispositioning processes taking place during agglomeration.

Acknowledgments

The authors are grateful to C.L. Jia, M. Lentzen, and H. Kohlstedt for inspiring discussions and enlightening comments.

References

Abelmann, L. & Lodder, C. (1997). Oblique evaporation and surface diffusion. *Thin Solid Films* **305**, 1–21.

Arakcheeva, A., Chapuis, G. & Grinevitch, V. (2002). The self-hosting structure of β-Ta. *Acta Cryst B* **58**, 1–7.

Boothroyd, C.B. (1998). Why don't high resolution simulations and images match? *J Microsc* **190**, 99–108.

Coene, W.M.J., Thust, A., Op De Beeck, M. & Van Dyck, D. (1996). Maximum-likelihood methods for focus-variation image reconstruction in high resolution transmission electron microscopy. *Ultramicroscopy* **64**, 109–135.

Face, D.W. & Prober, D.E. (1987). Nucleation of body-centred-cubic tantalum films with a thin niobium underlayer. *J Vac Sci Technol A* **5**, 3408–3411.

Feinstein, L.G. & Huttemann, R.D. (1973). Factors controlling the structure of sputtered Ta films. *Thin Solid Films* **16**, 129–145.

Gatan Inc. (1999). DigitalMicrograph 3.4 User's Guide. Pleasanton, CA: Gatan Inc.

Gupta, D. (1995). Diffusion in several materials relevant to Cu interconnection technology. *Mater Chem Phys* **41**, 199–205.

Haider, M., Rose, H., Uhlemann, S., Schwan, E., Kabius, B. & Urban, K. (1998). Electron microscopy image enhanced. *Nature* **392**, 768–769.

Hieber, K. & Mayer, N.M. (1982). Structural changes of evaporated tantalum during film growth. *Thin Solid Films* **90**, 43–50.

Hirsch, P., Howie, A., Nicholson, R., Pashley, D.W. & Whelan, M.J. (1965). *Electron Microscopy of Thin Crystals*. London: Butterworth.

Hübner, R., Hecker, M., Mattern, N., Hoffmann, V., Wetzig, K., Wenger, C., Engelmann, H.J., Wenzel, C., Zschech, E. & Bartha, J.W. (2003). Structure and thermal stability of graded Ta-TaN diffusion barriers between Cu and SiO_{2}. *Thin Solid Films* **437**, 248–256.

Hÿtch, M.J. & Stobbs, W.M. (1994). Quantitative comparison of high resolution TEM images with image simulations. *Ultramicroscopy* **53**, 191–203.

Jia, C.L., Lentzen, M. & Urban, K. (2004). High-resolution transmission electron microscopy using negative spherical aberration. *Microsc Microanal* **10**, 174–184.

Jiang, A., Yohannan, A., Nnolim, N.O., Tyson, T.A., Axe, L., Lee, S.L. & Cote, P. (2003). Investigation of the structure of β-tantalum. *Thin Solid Films* **437**, 116–122.

Klaver, P. & Thijsse, B. (2002). Thin Ta films: Growth, stability, and diffusion studied by molecular-dynamics simulations. *Thin Solid Films* **413**, 110–120.

Kwon, K.W., Lee, H.J. & Sinclair, R. (1999). Solid-state amorphization at tetragonal-Ta/Cu interfaces. *Appl Phys Lett* **75**, 935–937.

Laurila, T., Zeng, K., Kivilahti, K., Molarius, J. & Suni, I. (2000). Failure mechanism of Ta diffusion barrier between Cu and Si. *J Appl Phys* **88**, 3377–3384.

Lentzen, M., Jahnen, B., Jia, C.L., Tillmann, K. & Urban, K. (2002). High-resolution imaging with an aberration-corrected transmission electron microscope. *Ultramicroscopy* **92**, 233–242.

Moseley, P.T. & Seabrook, C.J. (1973). The crystal structure of β-tantalum. *Acta Cryst B* **29**, 1170–1171.

O'Keefe, M.A. & Kilaas, R. (1988). Advances in high-resolution image simulation. *Scan Microsc Suppl* **2**, 225–244.

Read, M.H. & Altman, C. (1965). A new structure in tantalum thin films. *Appl Phys Lett* **7**, 51–52.

Sajovec, F., Meuffels, P.M. & Schober, T. (1992). Structural and electrical properties of ion beam sputter deposited tantalum films. *Thin Solid Films* **219**, 206–209.

Stadelmann, P.A. (1987). EMS—A software package for electron diffraction analysis and HREM image simulation in materials science. *Ultramicroscopy* **21**, 131–145.

Stokes, R.J. & Evans, D.F. (1997). *Fundamentals of Interfacial Engineering*. New York: John Wiley & Sons.

Thust, A., Coene, W.M.J., Op De Beeck, M. & Van Dyck, D. (1996*a*). Focal-series reconstruction in HRTEM: Simulation studies on non-periodic objects. *Ultramicroscopy* **64**, 211–230.

Thust, A., Jia, C.L. & Urban, K. (2002). Extraction of imaging parameters from the object wave function in phase-retrieval electron microscopy. In *Proceedings of the 15th International Congress on Electron Microscopy*, Cross, R. (Ed.), vol. 3, pp. 167–168. Durban, South Africa: Microscopy Society of Southern Africa.

Thust, A., Overwijk, M.H.F., Coene, W.M.J. & Lentzen, M. (1996*b*). Numerical correction of lens aberrations in phase-retrieval HRTEM. *Ultramicroscopy* **64**, 249–264.

Tillmann, K., Thust, A. & Urban, K. (2004). Spherical aberration correction in tandem with exit-plane wave reconstruction: Interlocking tools for the atomic scale imaging of lattice defects in GaAs. *Microsc Microanal* **10**, 185–198.

Venables, J.A., Spiller, G.D.T. & Hanbücken, M. (1984). Nucleation and growth of thin films. *Rep Prog Phys* **47**, 399–459.

Westwood, W.D. (1973). X-ray analysis of tantalum films triode-sputtered in argon–oxygen mixtures. *Thin Solid Films* **15**, 15–30.

Westwood, W.D., Waterhouse, N. & Wilcox, P.S. (1975). *Tantalum Thin Films*. London: Academic Press.